PHOTONICS Research

Real-time collision dynamics of vector solitons in a fiber laser

Kangjun Zhao,[1] Chenxin Gao,[1] Xiaosheng Xiao,[2] and Changxi Yang[1,*]

[1]State Key Laboratory of Precision Measurement Technology and Instruments, Department of Precision Instruments, Tsinghua University, Beijing 100084, China
[2]State Key Laboratory of Information Photonics and Optical Communications, Beijing University of Posts and Telecommunications, Beijing 100876, China
*Corresponding author: cxyang@tsinghua.edu.cn

Received 30 October 2020; revised 21 December 2020; accepted 23 December 2020; posted 24 December 2020 (Doc. ID 413855); published 10 February 2021

Particle-like structures of solitons, as a result of the balance between dispersion and nonlinearity, enable remarkable elastic and inelastic soliton collisions in many fields. Despite the experimental observation of temporal vector-soliton collisions in birefringent fibers, collision dynamics of vector solitons in fiber lasers have not been revealed before, to the best of our knowledge. Here, the real-time spectral evolutions of vector solitons during collisions in a dual-comb fiber laser, which generates vector solitons with slightly different repetition rates, are captured by a time-stretch dispersive Fourier transform technique. We record the whole process of vector-soliton collisions, including the formation of weak pulses induced by cross-polarization coupling, opposite central wavelength shifts of both vector solitons, distinct intensity redistribution and dissipative energy, and gradual recovery to initial states. Furthermore, extreme collisions with strong four-wave mixing sidebands are observed by virtue of coherent coupling between the orthogonal polarization components of vector solitons. Numerical simulations match well with the experimental observations. The experimental and numerical evidences of vector-soliton collision dynamics could give insight into the understanding of nonlinear dynamics in fiber lasers and other physical systems, as well as the improvement of laser performance for application in dual-comb spectroscopy.

https://doi.org/10.1364/PRJ.413855

1. INTRODUCTION

Soliton collisions, as one of the most fascinating interactions in nonlinear systems, have been extensively investigated in the fields of metamaterials [1], photorefractive materials [2,3], Bose–Einstein condensates [4,5], and fiber optics [6,7]. In the framework of the nonlinear Schrödinger equation, due to their particle-like features, scalar solitons collide only by phase and position shifts with unaltered shape, amplitude, or speed after passing through one another [4,6]. As a remarkable contrast, collision interactions between vector solitons exhibit richer phenomena, such as intensity redistributions [8,9], energy-exchange interactions [2], and fractal structure [10]. Such wealthy nonlinear dynamics in collision of vector solitons paves the way for potential applications in all-optical logic and universal computation [11,12].

Optical fiber is an excellent platform for investigating the propagation and collision of vector solitons. To date, extensive theoretical and numerical but few experimental investigations have been reported to give insight into the intrinsic nature of the vector-soliton collision dynamics [6,8,10,13,14]. The first experimental observation of temporal vector-soliton collision was demonstrated in a linearly birefringent fiber, in which an intensity redistribution between both polarization components was observed before and after collision [6]. Nevertheless, visualized mutual spectral–temporal evolutions of both vector solitons during collision were not referenced. In addition, stable vector solitons in such a conservative system require only the balance between fiber nonlinearity and dispersion. Dissipative systems, such as mode-locked lasers, involve more rigorous requirements with another balance between gain and loss. Therefore, collision dynamics of vector solitons might characterize more marvelous features in mode-locked lasers than in birefringent fibers. More recent reports have shown that vector solitons with different group velocities can be steadily operated in each polarization component of optical fibers by inserting a segment of polarization-maintaining fiber (PMF) in a mode-locked fiber laser [15]. The slightly different repetition rates of both vector solitons lead to their mutual collisions from time to time. Although this fiber laser can act as an ideal candidate to investigate

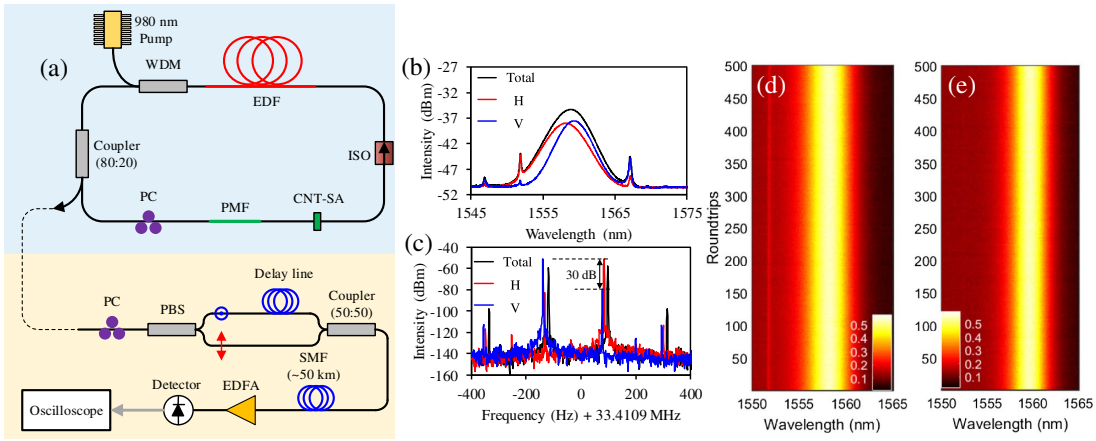

Fig. 1. Generation and characterization of two vector solitons with slightly different repetition rates from a mode-locked fiber laser. (a) Schematic of the mode-locked fiber laser (blue) and single-shot spectral measurement (orange). WDM, wavelength-division multiplexer; EDF, erbium-doped fiber; ISO, isolator; CNT-SA, carbon-nanotube saturable absorber; PMF, polarization-maintaining fiber; PC, polarization controller; PBS, polarization beam splitter; SMF, single-mode fiber; EDFA, erbium-doped fiber amplifier. (b), (c) Optical and radio frequency spectra of the two vector solitons before (black) and after (red and blue) passing through PBS. (d), (e) Stable single-shot spectra of the two vector solitons before collisions.

vector-soliton collisions, it remains unclear about the detailed collision dynamics so far.

The fast transient dynamics of soliton collisions in fiber lasers cannot be retrieved by conventional averaged optical spectral analyzers (OSAs) and autocorrelators, due to the limited measurement bandwidth. More recently, the time-stretch dispersive Fourier transform (TS-DFT) technique, developed for real-time spectral characterization, has been adopted to reveal the buildup and internal dynamics of soliton molecules [16–19], the behaviors of soliton buildup [20–22], and exotic dynamics of soliton explosions [23–26]. This technique has been demonstrated as a powerful tool for the measurement of rapid scalar soliton-collision processes [27,28]. Based on this excellent technique, we systematically investigated the buildup dynamics of asynchronous vector solitons in fiber lasers in our preliminary work [29].

Here, we experimentally and numerically investigate, with the help of the TS-DFT technique, the single-shot dynamics of vector-soliton collisions in a polarization-multiplexed mode-locked fiber laser. Before collision, another two weak pulses are formed by cross-polarization coupling between the orthogonal polarization components. When overlapping with each other, both vector solitons experience opposite central wavelength shifts induced by cross-phase modulation (XPM). A distinct intensity difference in the weak pulse before and after collision implies intensity redistribution. Moreover, the nonconservative total energy of both vector solitons occurs during the collision process. Eventually, both solitons recover to their initial states after several hundred roundtrip (RT) evolutions. Under specific conditions, extreme collisions with strong four-wave-mixing (FWM) sidebands are observed by virtue of coherent coupling, which extends the scenario of FWM sideband generation from steady mode locking to transient collisions. Our study might not only provide deep insight into the collision dynamics of vector solitons, but also contribute to improving the laser design for its application prospect in dual-comb spectroscopy [30–32].

2. GENERATION OF VECTOR SOLITONS WITH DIFFERENT REPETITION RATES

We generated two nearly orthogonally polarized vector solitons with different repetition rates in a polarization-multiplexed erbium-doped mode-locked fiber laser. The experimental setup is depicted in Fig. 1(a) (see Appendix A for detailed information). Asynchronous vector solitons are obtained by increasing the pump power to 70 mW and properly tuning the polarization controller (PC). When we trigger one pulse train, another one periodically moves on the oscilloscope. Figures 1(b) and 1(c) show the polarization-resolved optical and radio frequency (RF) spectra, assisted by a PC and a polarization beam splitter (PBS). Both solitons exhibit overlapped spectra [Fig. 1(b)], near repetition rate of 33.4109 MHz, and slight difference of 217 Hz [Fig. 1(c)]. The RF spectra of both vector solitons could be suppressed with a 30 dB polarization extinction ratio (PER) but not be eliminated, indicating their close-to-orthogonal polarizations [15,29]. The central wavelengths and 3 dB bandwidths of these vector solitons are 1558.3 and 5 nm, 1559.7 and 4.1 nm, respectively. Thus, the TS-DFT system could stretch them to 4.25 and 3.49 ns, respectively, in accordance with the scale of time-to-wavelength mapping. In addition, the mismatched repetition rates lead to a mutual collision with a period of 4.6 ms in the laser cavity. Figures 1(d) and 1(e) present the stable spectral evolutions over 500 RTs in two-dimensional color plots before collisions, indicating little interaction between the two vector solitons when they are far from each other.

3. EXPERIMENTAL OBSERVATIONS

A. Moderate Collisions

A vector soliton in fast axis exhibits larger group velocity than the other one, consequently leading to their being close, overlapped, and far away. In consideration of periodic boundary conditions of self-consistency in laser ring cavities, mode-locking states of vector solitons, before and after collision, need to be maintained.

As we can see in Fig. 2(a), in the collision process measured by TS-DFT, stable mode locking before collision shows intensity equivalent to recovered stable mode locking after collision, which is also confirmed by the nearly overlapped spectral information before (10–10.1 μs) and after collision (80–80.1 μs) in Fig. 2(b). Other imperceptible evidences can also be found in Figs. 2(j) and 2(k) with identical central wavelength and energy before and after collision. In contrast, the most fascinating aspect is the collision process when temporal vector solitons overlap with each other, accompanied by dramatic spectral and temporal variations by XPM. Figure 2(c) presents measurements of their spectral information with changed intensities and shapes during collision (50–50.1 μs).

We then plot their single-shot spectral interferograms and Fourier transformed field autocorrelations over 3000 RTs [Figs. 2(d), 2(f), and 2(h)] to reveal the universal dynamics of vector-soliton collisions. Figures 2(e), 2(g), and 2(i), including the most representative colliding information, are the enlarged views of Figs. 2(d), 2(f), and 2(h), respectively, from 1630th to 1800th RTs. Due to its shorter central wavelength, broader spectral bandwidth, and higher repetition rate [Figs. 1(b) and 1(c)], the vector soliton in Fig. 2(e) (horizontal polarization) holds faster moving speed than the other one [vertical polarization in Fig. 2(g)]. In this scenario, the horizontally polarized vector soliton catches up with and passes through the vertically polarized one. During the 1630th to 1660th RTs, dense spectral interference patterns of both vector solitons indicate the appearance of a weak pulse at each polarization component (these weak pulses are formed by cross-polarization coupling between the orthogonal polarization components in

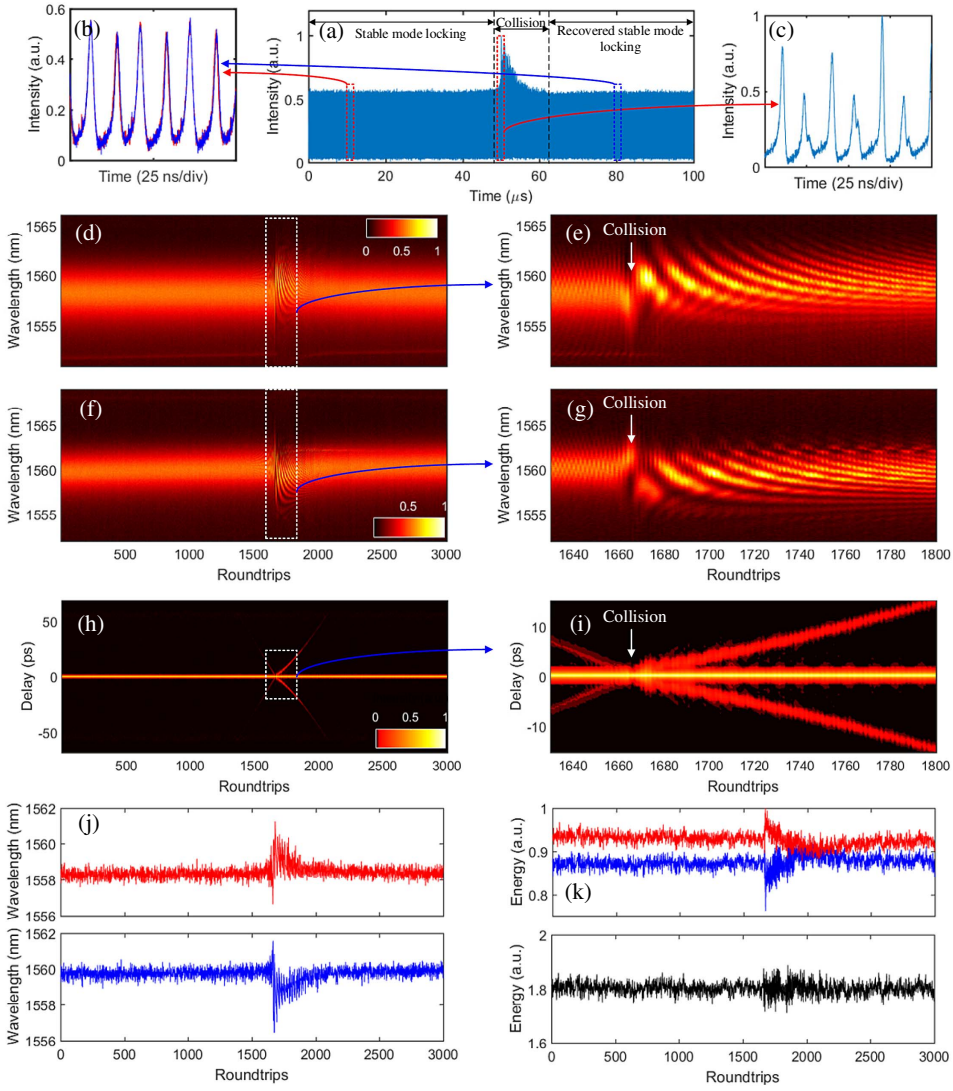

Fig. 2. Experimental real-time characterization of moderate collision of vector solitons. (a) Single-shot collision dynamics of vector solitons by the TS-DFT technique. (b), (c) Close-up of the data in (a) before, after, and during collision, respectively. (d), (f) Real-time spectral evolutions of the two vector solitons during collisions. (e), (g) Close-up of the data in (d), (f), respectively. (h) Field autocorrelation trace in (f) via Fourier transform. (i) Close-up of the data in (h). (j) Central wavelength evolutions of vector solitons (d), (f) during collisions. (k) Energies of both vector solitons (red and blue) and their total energy (black).

Section 4), as evidence of two weak peaks symmetrically located on both sides of an intense peak from the field autocorrelation trace in Fig. 2(i). Note that the 0.14 nm spectral resolution of our DFT system determines its recording limitation of pulse separation of ∼57 ps. Even so, it has little influence on the detailed collision process due to the short pulse spacing during collision. The separation between the dominant and weak pulses linearly decreases at a speed of 193.7 fs/RT, corresponding to their repetition rate difference of ∼216 Hz, indicating that the weak pulse has the same group velocity as the dominant vector soliton in another polarization axis. During the 1660th to 1666th RTs, central wavelength drifts in opposite directions [Figs. 2(e) and 2(g)] could be interpreted as a result of temporal overlap-induced XPM. The leading edge of the horizontally polarized vector soliton overlaps with the trailing edge of the vertically polarized vector soliton. Thus, the XPM-induced chirps of horizontally and vertically polarized vector solitons are positive and negative, respectively, leading to their blue- and red-shift spectra. In addition, frequency shifts increase with the cavity RTs owing to their stronger and stronger temporal overlap.

The collision position is at the 1666th RT. Remarkably, there are both suddenly opposite central wavelength shifts from 1666th to 1667th RTs, ascribed to the exchange of their overlapped parts, i.e., the trailing and leading edges of the horizontally and vertically polarized vector solitons, respectively, are overlapped after collision. Predominant shifts of the fringe patterns from red to blue and gradually slowing down can be observed during the 1667th to 1800th RTs, representing monotonous changes and tendency to an extremum of the relative phase between the weak pulse and identically polarized vector soliton [33]. Also, the denser and denser spectral interference patterns [Figs. 2(e) and 2(g)] correspond to their larger and larger temporal separations [Fig. 2(i)]. After collision, the speed of walking off between both vector solitons is slower than that before, and experiences the processes of acceleration and rapid recovering. Similar to soliton trapping, the two orthogonally polarized vector solitons shift their central wavelengths in opposite directions, as depicted in Fig. 2(j). The close central wavelengths decrease their group velocity difference, leading to stronger soliton–soliton interactions induced by XPM. Eventually, gradually reduced interactions along with their increased temporal separation result in the recovery, including the central wavelengths and group velocity difference.

Figure 2(k) shows the energy evolutions of both vector solitons during the entire collision process. Due to the inevitable electronic noise, the energy profiles are not smooth. Nevertheless, we can still observe the clear energy redistributions with an unfixed total energy during collision, in accordance with the numerical simulations [shown below in Fig. 4(g)]. Compared with the conservative collisions in passive optical fiber, our dissipative fiber laser can support the growth and consumption of total energy of both vector solitons (see Appendix C).

B. Extreme Collisions

As depicted in Fig. 3(a), extreme collisions, a mass of intense peaks locating on a vector soliton after collision (55–75 μs), occur when properly tuning the PC in the laser cavity. A zoom-in of the extremely colliding region (63.95–64.05 μs) is shown in Fig. 3(b). Obviously, narrow peaks with unequal intensities appear only on the vertically polarized vector soliton, which features stronger spectral peak power and narrower spectral bandwidth than the other one. It is worth noting that the narrow peaks, propagating together with the vector soliton, are coherent components rather than continuous-wave emission; otherwise, they would disperse and disappear after TS-DFT [34].

Analogous to the moderate collision, the entire spectral evolutions of extreme collisions in Figs. 3(c) and 3(e) include stable mode locking before collision, gradually and suddenly opposite central wavelength shifts, a gradual recovery process, and recovered stable mode locking after collision. The differences are the nearly periodic narrow peaks during the recovery process [Fig. 3(f)], with a period of 15 RTs, in accordance with its periodic intensity field autocorrelation trace in Fig. 3(h). As a contrast, another polarized vector soliton presents a smooth evolution without any tendency of narrow peaks in Fig. 3(d). The detailed explanations are explored in Section 4.

4. NUMERICAL SIMULATIONS

A. Moderate Collisions

To give more insight into the collision dynamics of vector solitons in mode-locked fiber lasers, the split-step Fourier method is adopted to solve the coupled Ginzburg–Landau equations in a lumped propagation model [35] (see Appendix B). Numerical simulations start from two weak pulses located at the fast and slow axes of the cavity, with a temporal interval of 280 ps, to speed up the convergence of our simulations. Both pulses converge into their stable solutions after 400 RT circulations. The initial front pulse is located at the fast axis; thus, the two pulses are close to each other and collide at the ∼1150th RT. By appropriately setting the PC, moderate and extreme collision dynamics of vector solitons, analogous to the experiments, can be reproduced. We first set $\theta = 0.005\pi$ and $\varphi = 0.55\pi$; similar opposite central wavelength shifts and recovery process can be obtained, as depicted in Figs. 4(a1), 4(a2), 4(b1), and 4(b2). It is worth noticing that a notable rebuilding process of Kelly sidebands (annihilating, rebuilding, and gradually recovering) [27] can be observed in our simulations. However, the reconstructed Kelly sidebands of vector solitons in the slow axis [Fig. 4(e2)] exhibit weaker intensity than the other one [Fig. 4(e1)], which can be explained by gain competition between them: in front of the vector soliton in the slow axis after collision, another disturbed soliton in the fast axis undergoes stronger gain, facilitating its spectral evolution including the buildup of new sidebands. The soliton spectra overlap with their Kelly sidebands, inducing the interference patterns on Kelly sidebands. In addition, central wavelength shifts of vector solitons change the phase-matching conditions of constructive interference between dispersive waves and solitons, leading to the opposite rebuilding positions of their Kelly sidebands.

The temporal evolutions of both vector solitons during collision, which cannot be measured directly by the TS-DFT technique, provide further insight into the collision dynamics. The collision position is at the 150th RT, as illustrated in Fig. 4(c), of temporal evolution of the vector soliton in the fast axis.

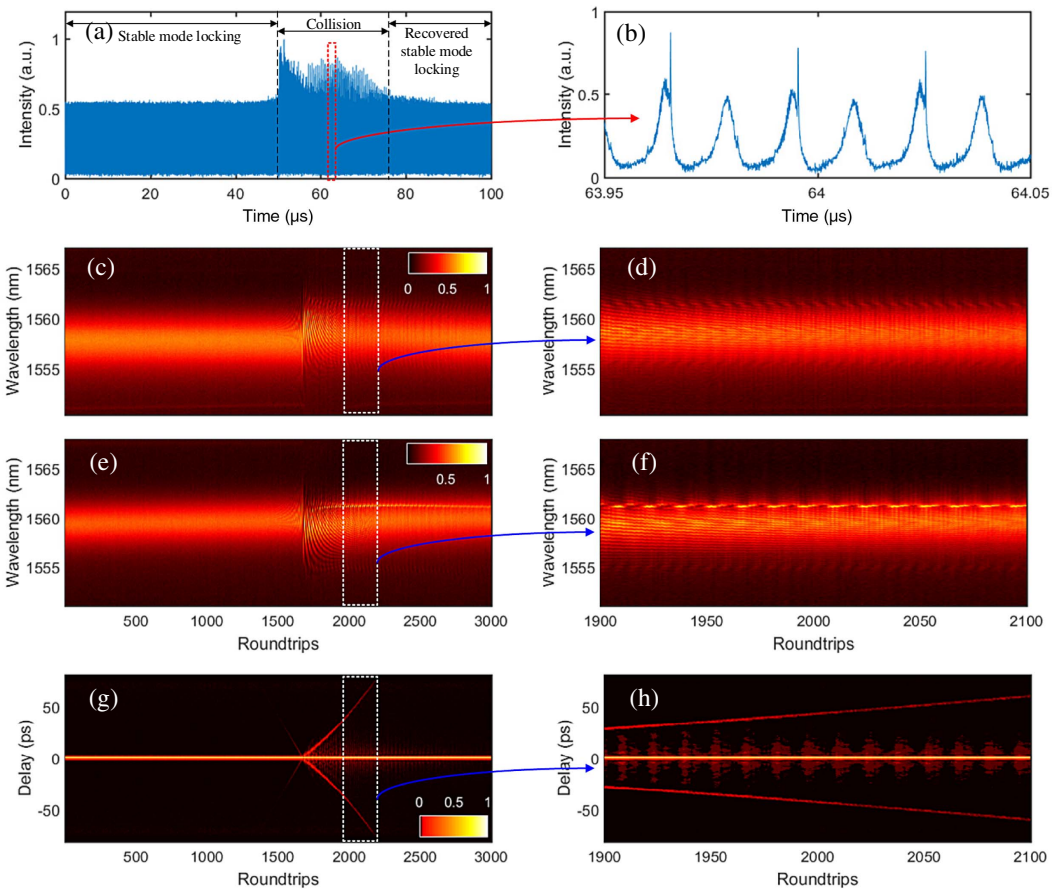

Fig. 3. Experimental real-time characterization of extreme collision of vector solitons. (a) Single-shot collision dynamics of vector solitons by the TS-DFT technique. (b) Close-up of the data in (a) after collision. (c), (e) Real-time spectral evolution of the two vector solitons during collisions. (d), (f) Close-up of the data in (c) and (e), respectively. (g) Field autocorrelation trace in (e) via Fourier transform. (h) Close-up of the data in (g).

Remarkably, temporal shifts from the 149th to 150th RTs move faster than before [inset in Fig. 4(c)], which could be attributed to the increased group velocity difference between vector solitons induced by opposite spectral shifts [Figs. 4(b1) and 4(b2)]. After collision, another pulse clearly appears at each polarization component. Actually, the weak pulse has also existed before collision, but is not shown in Fig. 4(c) due to its weak intensity. To better show it, we plot the fast axis field autocorrelation trace and tune the upper limit of the colorbar, as sketched in Fig. 4(d). Simulations show that the weak pulse, trapping another axis vector soliton to propagate together, is stable before collision, indicating an incomplete coincidence between polarization directions of the vector solitons and principal axes of the fibers. To explore whether the weak pulse is induced by the dominant soliton through XPM, we deliberately remove the XPM terms in our simulations. It is noticed that the weak pulse continuously damps and eventually disappears in this case. When re-adding the XPM terms, the weak pulse gradually arises and stabilizes again, indicating that the induced weak pulse is formed by cross-polarization coupling between the orthogonal polarization components [36]. A distinct intensity difference in the weak pulse before and after collision [Fig. 4(d)] implies intensity redistribution [2,8,9].

As was expected, vector-soliton collisions also result in dispersive wave shedding, as depicted in Fig. 4(f). Both the dominant soliton and weak pulse symmetrically shed some energy in the form of collision-induced dispersive waves, leading to complicated patterns between them due to the superposition of dispersive waves. Subsequently, the dispersive waves are broadened and weakened by fiber dispersion during circulation in the cavity. Far away from each other between the dominant soliton and weak pulse, the dispersive wave shedding becomes weaker and weaker and gradually disappears for recovery to the initial state before collision. The energy evolutions in Figs. 4(g1) and 4(g2) also match well with the experiments [Fig. 2(k)].

B. Extreme Collisions

Extreme collisions of vector solitons were well reproduced in our simulations when setting $\theta = 0$ and $\varphi = 0.2\pi$, as shown in Fig. 5. Periodic narrow peaks at the wavelength of 1562 nm are presented in the slow axis after 250 RTs [Figs. 5(a2) and 5(b2)], with no signs in the fast axis [Figs. 5(a1) and 5(b1)]. Figures 5(c1) and 5(c2), at the 498th RT, show the cross-sections of both vector solitons' spectra. The modulations on both spectra correspond to the two separated pulses (dominant soliton and weak pulse) in the temporal domain. A larger

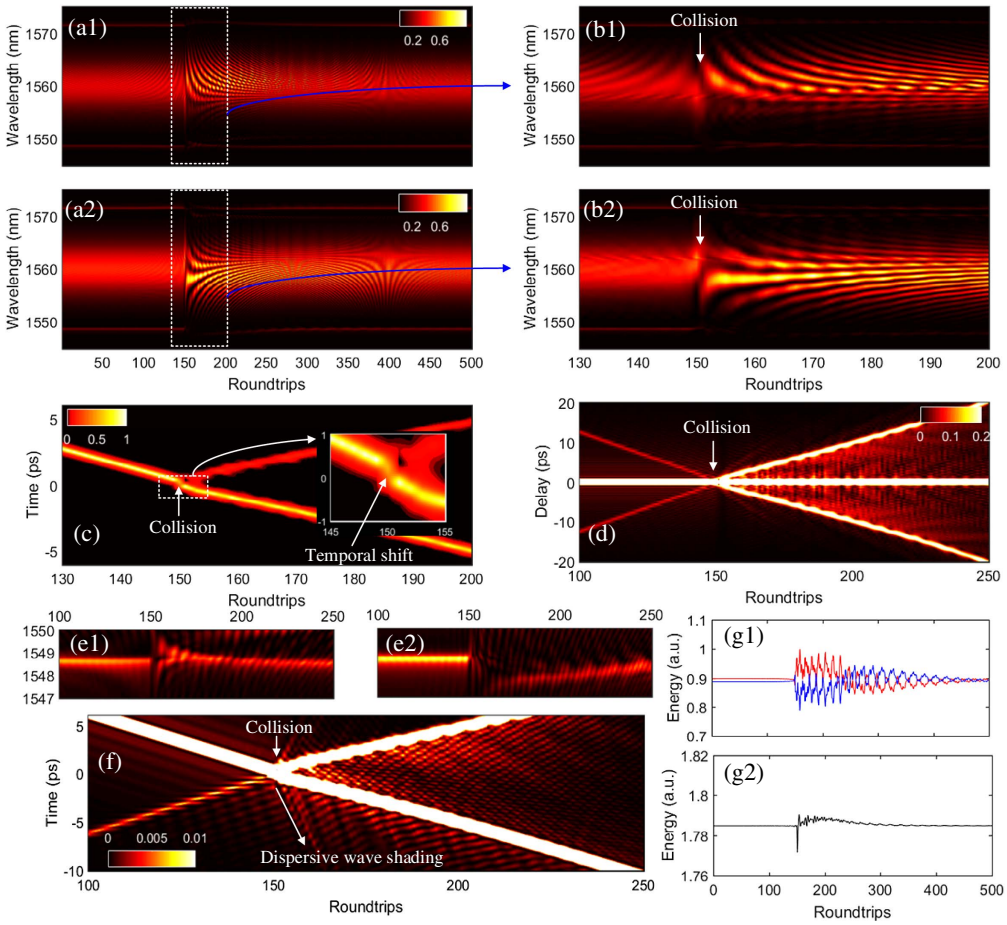

Fig. 4. Numerical simulations of moderate collision of vector solitons. (a1), (b1), (e1) Spectral evolution, close-up of the data in (a1), and Kelly sideband rebuilding process of vector soliton in fast axis, respectively. (a2), (b2), (e2) Corresponding spectral evolution, close-up of the data in (a2), and Kelly sideband rebuilding process of vector soliton in slow axis, respectively. (c), (d), (f) Temporal evolution, field autocorrelation trace, and dispersive wave shedding of vector soliton in fast axis, respectively. (g1), (g2) Energy evolutions of vector solitons in fast (red) and slow (blue) axes, and total energy evolution. Inset: close-up of the data in (c).

spectral fringe modulation depth in the slow axis indicates a stronger weak pulse than the one in the fast axis, which is verified by their temporal traces in blue boxes in Figs. 5(d1) and 5(d2). To better display the weak pulses, we present only a small part of the normalized dominant solitons [red boxes in Figs. 5(d1) and 5(d2)]. To further explore a profound understanding of the generation of narrow peaks, the temporal traces of the dominant soliton and weak pulse are Fourier transformed to investigate their optical spectra. A strong spectral sideband at the wavelength of 1562 nm [blue curve in Fig. 5(e2)] matches well with the location of the narrow peaks in Fig. 5(c2), and is in striking contrast to the smooth spectrum of the red curve. More scrupulously, the approximately periodic sideband evolution [Fig. 5(f2)] and stable spectral evolution [Fig. 5(f1)] during the 490th to 500th RTs, indicate sharply that narrow peaks indeed arise from the notable spectral sideband of the weak pulse. Specifically, the strong spectral sideband at 1562 nm is not a Kelly sideband owing to its unmatched spectral interval (4.5 nm) between the soliton central wavelength and spectral sideband. According to Ref. [37], we can derive that the wavelength offset between the first-order Kelly sideband and soliton central wavelength is about 12 nm, matching well with the spectral sideband at 1570 nm with 12.3 nm offset [blue curve in Fig. 5(e2)]. Further insight into the spectral sideband at 1562 nm is provided by deliberately removing the coherent coupling terms in our simulations. Notably, the Kelly sideband at 1570 nm can always be observed, but no extra spectral sideband at 1562 nm occurs. It occurs again when considering the coherent coupling terms, manifesting that coherent coupling between the orthogonal polarization components plays a crucial role in the FWM spectral sideband [38,39]. The dominant vector soliton in the fast axis traps the weak pulse in the slow axis to propagate together, and their coherent coupling generates the strong FWM sideband in the weak pulse. In contrast, the weaker pulse in the fast axis, two orders of magnitude smaller than that in Fig. 5(d2), is not able to generate an obvious FWM sideband. The relative intensities of the weak pulses on both polarization axes are strongly dependent on the net cavity birefringence induced by the PC. Numerical simulations also show that the weaker pulse in the fast axis could have much stronger itensity than the one in the slow axis by setting $\theta = 0$ and $\varphi = 0.4\pi$.

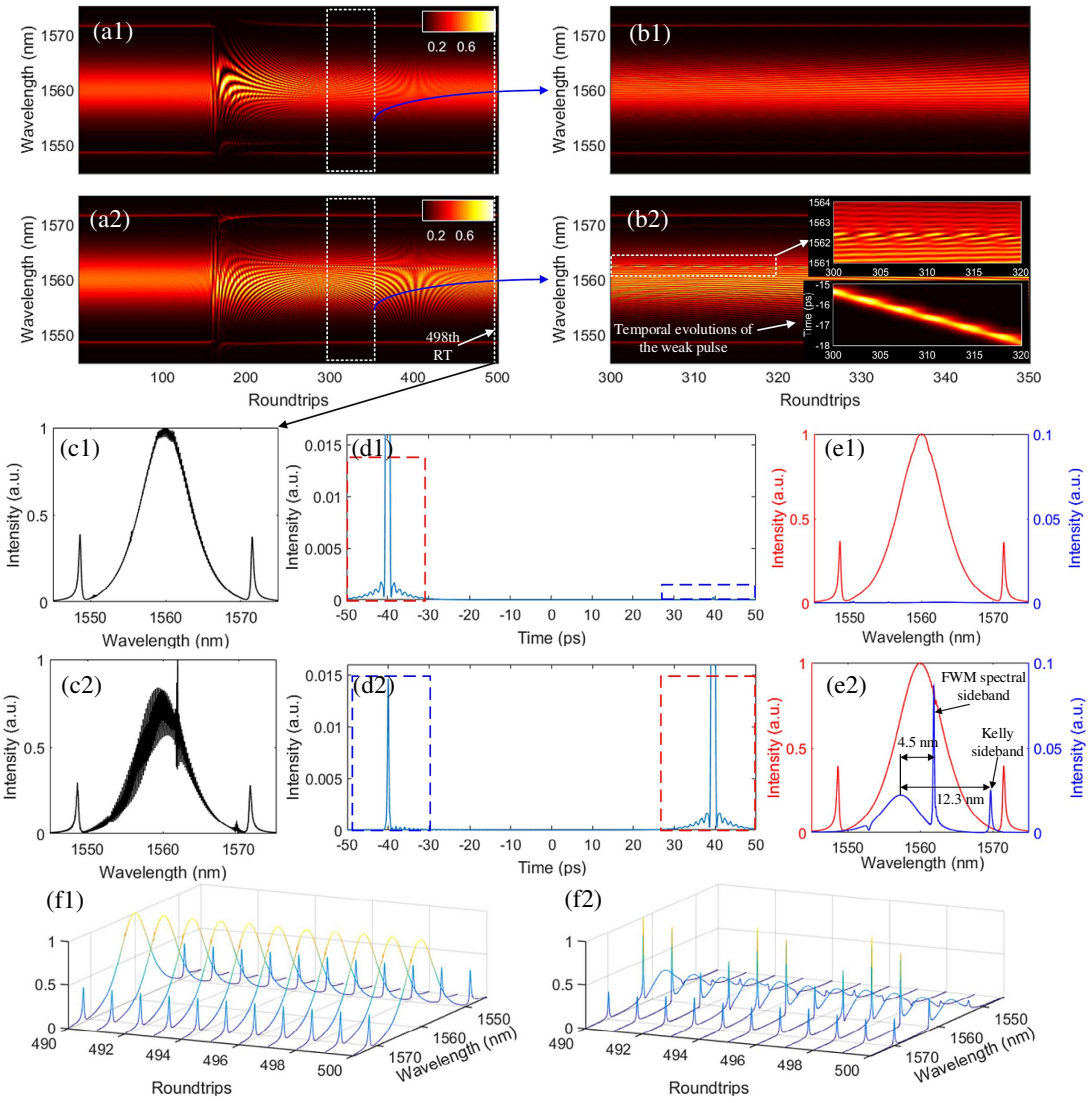

Fig. 5. Numerical simulations of extreme collision of vector solitons. (a1), (a2) Spectral evolutions of the two vector solitons during collisions. (b1), (b2) Close-up of the data in (a1), (a2), respectively. (c1), (c2) Optical spectra at the 498th RT. (d1), (d2) Temporal traces at the 498th RT. (e1), (e2) Optical spectra of the dominant soliton [red curves, corresponding to the temporal traces in red boxes in (d)] and weak pulse [blue curves, corresponding to the temporal traces in blue boxes in (d)] by Fourier transform. (f1), (f2) Spectral evolutions of the dominant soliton and weak pulse, respectively, from the 490th to 500th RTs in (a2). Insets in (b2): close-up of the spectral evolutions (upper right) and temporal evolutions of the weak pulse (bottom right) from the 300th to 320th RTs.

Both experiments [Fig. 3(f)] and simulations [Figs. 5(b2) and 5(f2)] present the quasi-periodic intensity evolutions of the FWM sideband. The temporal evolutions of the weak pulse in the slow axis [bottom right inset in Fig. 5(b2)] behave analogously to soliton pulsation, which has been extensively investigated in mode-locked lasers [40–42]. Given that, regardless of

Table 1. Parameters Used in the Simulations

OC	SA	SMF	PMF	EDF
$T = 0.2$	$T_0 = 0.6$ $\Delta T = 0.05$ $P_{sat} = 10$ W	$L = 5.3$ m $\beta_2 = -22.9$ ps$^2 \cdot$ km^{-1} $\gamma = 1.3$ W$^{-1} \cdot$ km^{-1} $L_B = 5$ m	$L = 0.2$ m $\beta_2 = -22.9$ ps$^2 \cdot$ km^{-1} $\gamma = 1.3$ W$^{-1} \cdot$ km^{-1} $L_B = 4.4$ mm	$L = 0.5$ m $\beta_2 = 11.4$ ps$^2 \cdot$ km^{-1} $\gamma = 1.3$ W$^{-1} \cdot$ km^{-1} $L_B = 5$ m $g_0 = 12$ m^{-1} $E_{sat} = 130$ pJ Gaussian shape FWHM = 20 nm

the negligible intensity change in the dominant soliton, the coherent coupling term [Eq. (B1) in Appendix B] is proportional to the electric field amplitude, and the quasi-periodic FWM sidebands can be traced to the quasi-periodic intensity variations of the weak pulse.

5. DISCUSSION AND CONCLUSION

A mode-locked fiber laser, as a complicated nonlinear dissipative system, provides a unique opportunity for exploring rich interactions between solitons. Our polarization-multiplexed mode-locked fiber laser with strong and weak birefringence in PMF and single-mode fiber (SMF), respectively, could be considered as a birefringence-managed fiber cavity within periodic gain and loss. Strong birefringence in PMF facilitates the generation of close-to-orthogonal vector solitons with slightly different repetition rates. The non-orthogonal polarization between both vector solitons could lead to cross-talk in each polarization. The 30 dB PER in Fig. 1(c) indicates that there could be 0.1% power of the dominant pulse located on the orthogonally polarized axis. Numerical simulations in Figs. 5(d1) and 5(d2) show that the intensity of the weak pulse in the slow axis is about 1.5% of the dominant pulse in the fast axis, indicating that there is little influence of cross-talk on the physical mechanism of the generated weak pulse. In addition, numerical simulations match well with the experiments, indirectly indicating little influence. The longer the PMF utilized in the fiber cavity, the larger the repetition rate difference between vector solitons. Both a small repetition rate difference (217 Hz in our experiments) and weak birefringence in SMF extend the interaction length between vector solitons. According to Ref. [27], the interaction length between vector solitons in our experiments could be approximated to 34.5 m, corresponding to an interaction time of 172 ns. Such a long soliton mutual interaction time enhances the nonlinear phase accumulation of both vector solitons during collision, inducing fascinating moderate and extreme collision dynamics. Extreme collision with FWM sidebands can be derived from the phase matching of both polarization components, which is strictly dependent on the net cavity birefringence. By properly adjusting the net cavity birefringence through the PC, both polarization components of the dominant vector soliton and the weak pulse might satisfy the phase-matching condition, leading to the generation of FWM sidebands. When far away from the phase-matching condition by tuning the PC, the collision dynamics presents moderate collisions. Compared to the vector soliton collision in a conservative system [6], degenerate FWM induced by the coherent coupling term in Eq. (B1) must be retained due to the sub-picosecond soliton pulses and dominant low birefringence in our fiber laser, leading to peculiar FWM spectral sidebands in an extreme collision process. When increasing the cavity length to dozens of meters or even more, the FWM sideband predictably disappears during vector soliton collisions, which we will investigate in future work. Moreover, temporal intensity and central wavelength in each soliton recover to their original status after collision due to the self-consistent conditions of the laser cavity, as shown in Appendix C.

It deserves to be mentioned that FWM spectral sidebands were observed only in steady operations of vector solitons in weakly birefringent mode-locked fiber lasers [38,39]. Our new findings of vector-soliton-collision-induced generation of FWM spectral sidebands could extend the dynamics of soliton–soliton interactions. Such transient dynamics cannot be resolved by conventional OSA, indicating the powerful ability of the TS-DFT technique in investigations of real-time spectral evolutions of dissipative solitons.

Our polarization-multiplexed mode-locked fiber laser can generate vector solitons with slightly different repetition rates, which has potential application in dual-comb spectroscopy. The configuration of dual-comb spectroscopy often consists of signal and reference arms, and the normalized transmission of the sample can be extracted by comparing the signal and reference spectra with heterodyne detections [43]. If considering the ideal case of the same collision process between both vector solitons during each collision in the fiber laser, the disturbances of their transient optical spectra induced by soliton collisions do not influence the measurement precision because of the approach of calibrating the real-time reference spectra. However, each collision process cannot be ensured to be absolutely the same, due to the environment perturbation, such that the signal-to-noise ratio of the measurement might decrease when adopting a coherent average. This could be resolved by several approaches, such as the real-time detection of repetition rate of the interferogram or correction algorithm [32].

In conclusion, we have explored the real-time moderate and extreme collision dynamics of vector solitons by the TS-DFT technique in a polarization-multiplexed mode-locked fiber laser. Cross-polarization coupling between the orthogonal polarization components of vector solitons induces another two weak pulses, and they experience distinct intensity redistribution after collision. Opposite central wavelength shifts, a gradual recovery process, and eventually recovering to their initial states of both vector solitons occur during collision. Furthermore, coherent coupling between the orthogonal polarization components of vector solitons can also lead to strong FWM sidebands. We believe that our results not only provide new perspectives in the collision dynamics of vector solitons in dissipative systems, but also pave the way towards the physical understanding of complex nonlinear science.

APPENDIX A: EXPERIMENTAL SETUP

1. Mode-Locked Fiber Laser

A 0.5 m erbium-doped fiber (EDF, LEKKI Er110-4/125) is backward-pumped by a 980 nm laser diode via a wavelength-division multiplexer (WDM). The saturable absorber (SA) of a carbon nanotube (CNT) is adopted in the laser cavity to assist mode locking. A polarization-independent isolator (ISO) ensures the unidirectional operation of the laser, and an optical coupler extracts 20% intracavity power for measurement. The most important part of the cavity is a 0.2 m piece of PMF with a beat length of ~4.4 mm, providing a local strong birefringence to facilitate the generation of asynchronous vector solitons. Propagations in fast and slow axes of PMF induce slightly mismatched repetition rates of both vector solitons, and lead to their inevitable collisions. A PC is utilized to

optimize the mode-locking state. The rest of the cavity is all SMF-28e. The total cavity length is ~6 m, corresponding to a net cavity dispersion of −0.12 ps^2.

2. TS-DFT and Measurement Systems

The single-shot spectral measurement based on the TS-DFT technique consists of a ~50 km length of SMF with a total dispersion of −1150 ps^2 to stretch the ultrashort pulses, a homemade EDF amplifier (EDFA) to compensate for fiber loss, and a high-speed oscilloscope (Keysight DSOS804A, 8 GHz bandwidth) with a fast photodetector (PD, ET-5000F, 12 GHz bandwidth) to produce data acquisition. Thus, the scale of time-to-wavelength mapping and the spectral resolution are 0.85 ns/nm and ~0.14 nm, respectively. To avoid temporal overlap between both vector solitons when colliding, a PBS and a 3 m SMF are employed to absolutely separate them and introduce a time delay. Then, these two time-delay pulses are combined by a 50/50 coupler and detected by the same PD. In addition to the single-shot spectral measurement system, conventional OSA (Yokogawa AQ6375) and RF signal analyzers (Agilent N9020 A) are also utilized to characterize the mode-locked pulses.

APPENDIX B: NUMERICAL SIMULATION MODEL

To give more insight into the collision dynamics of vector solitons in mode-locked fiber lasers, the split-step Fourier method is adopted to solve the coupled Ginzburg–Landau equations in a lumped propagation model [35]:

$$\begin{aligned}\frac{\partial u}{\partial z} &= i\beta u - \delta\frac{\partial u}{\partial t} - \frac{i\beta_2}{2}\frac{\partial^2 u}{\partial t^2} + i\gamma\left(|u|^2 + \frac{2}{3}|v|^2\right)u \\ &\quad + \frac{i\gamma}{3}v^2u^* + \frac{g}{2}u + \frac{g}{2\Omega_g^2}\frac{\partial^2 u}{\partial t^2}, \\ \frac{\partial v}{\partial z} &= -i\beta v + \delta\frac{\partial v}{\partial t} - \frac{i\beta_2}{2}\frac{\partial^2 v}{\partial t^2} + i\gamma\left(|v|^2 + \frac{2}{3}|u|^2\right)v \\ &\quad + \frac{i\gamma}{3}u^2v^* + \frac{g}{2}v + \frac{g}{2\Omega_g^2}\frac{\partial^2 v}{\partial t^2},\end{aligned} \tag{B1}$$

where u and v are the slowly varying pulse envelopes of fast and slow axes of the cavity, respectively. $2\beta = 2\pi\Delta n/\lambda = 2\pi/L_B$ and $2\delta = \beta\lambda/\pi c$ are the wave number difference and inverse group velocity difference, respectively. L_B is the beat length, β_2 is the group velocity dispersion, γ is the Kerr nonlinear coefficient, $g = g_0\exp[-\int(|u|^2 + |v|^2)\mathrm{d}t/E_{\mathrm{sat}}]$ is the gain, and Ω_g is the gain bandwidth of the gain fiber. g_0 and E_{sat} are the small signal gain and gain saturation energy, respectively. The transmission of the SA is modeled by

$$T = T_0 - \frac{\Delta T}{1 + (|u|^2 + |v|^2)/P_{\mathrm{sat}}}, \tag{B2}$$

where T_0 denotes the saturable transmission, ΔT is the modulation depth, and P_{sat} is the saturation power. In addition, the PC is modeled by the multiplication of the vector field by the following Jones matrix:

$$J_{\mathrm{PC}} = \begin{bmatrix}\cos\theta & -\sin\theta \\ \sin\theta & \cos\theta\end{bmatrix}\begin{bmatrix}e^{i\varphi/2} & 0 \\ 0 & e^{-i\varphi/2}\end{bmatrix}\begin{bmatrix}\cos\theta & \sin\theta \\ -\sin\theta & \cos\theta\end{bmatrix}, \tag{B3}$$

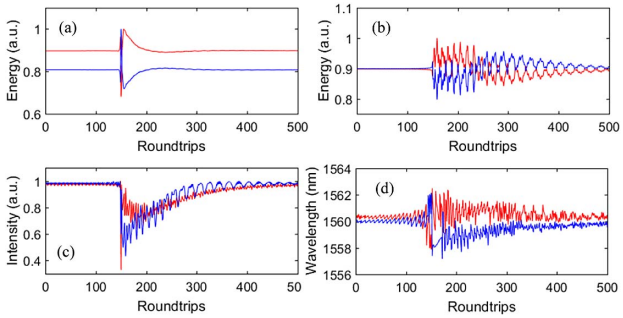

Fig. 6. Numerical simulation results of (a), (b) total energy in each soliton and in each component, (c) temporal intensity, and (d) central wavelength in each soliton.

where φ is the phase delay caused by the PC, and θ is the angle of the PC defined with respect to the fast axis of the fiber. The parameters, according to experimental conditions, used in the numerical simulations are listed in Table 1.

APPENDIX C: ENERGY REDISTRIBUTIONS IN MODERATE COLLISIONS

Reference [6] points out that the total energy in each soliton and in each component is conserved when two vector solitons collide with each other in birefringent fiber. To explore the similarities and differences between vector solitons colliding in the conservative system mentioned above and in the dissipative system of our fiber laser, we numerically demonstrate the total energy in each soliton [Fig. 6(a)] and in each component [Fig. 6(b)] during collision. Simulation parameters are the same as moderate collisions in Fig. 4. It is similar to Ref. [6], in that the total energy in each soliton and in each component does not change before and after collision, despite different recovering time. However, differences are presented in the temporal intensity and central wavelength in each soliton. Energy redistributions and wavelength shifts of both vector solitons are significant features in Ref. [6], while both of them recover to their original status after collision in our fiber laser [Figs. 6(c) and 6(d)] due to the self-consistent conditions of the laser cavity. Also, remarkable energy redistributions of vector solitons occur in violent collisions [from the 100th to 200th RTs in Fig. 6(a)]. However, their total energy [Fig. 4(g2)] is not conserved to a fixed value, indicating that this dissipative system under collision-induced perturbations automatically supplies the energy of both vector solitons, which is an evident distinction in a conservative system without any additional energy source.

Funding. National Natural Science Foundation of China (51527901, 61975090).

Acknowledgment. The authors are grateful for the fruitful discussions with Xiaoming Qiu (Peking University) and Frank Wise (Cornell University) on this paper.

Disclosures. The authors declare that they have no conflicts of interest related to this work.

REFERENCES

1. B. Deng, V. Tournat, P. Wang, and K. Bertoldi, "Anomalous collisions of elastic vector solitons in mechanical metamaterials," Phys. Rev. Lett. **122**, 044101 (2019).
2. C. Anastassiou, M. Segev, K. Steiglitz, J. Giordmaine, M. Mitchell, M. Shih, S. Lan, and J. Martin, "Energy-exchange interactions between colliding vector solitons," Phys. Rev. Lett. **83**, 2332–2335 (1999).
3. F. Xin, M. Flammini, F. Mei, L. Falsi, D. Pierangeli, A. Agranat, and E. Delre, "Observation of extreme nonreciprocal wave amplification from single soliton-soliton collisions," Phys. Rev. A **100**, 043816 (2019).
4. J. Nguyen, P. Dyke, D. Luo, B. Malomed, and R. Hulet, "Collisions of matter-wave solitons," Nat. Phys. **10**, 918–922 (2014).
5. S. Stellmer, C. Becker, P. Panahi, E. Richter, S. Dorscher, M. Baumert, J. Kronjager, K. Bongs, and K. Sengstock, "Collisions of dark solitons in elongated Bose-Einstein condensates," Phys. Rev. Lett. **101**, 120406 (2008).
6. D. Rand, I. Glesk, C. Bres, D. Nolan, X. Chen, J. Koh, J. Fleischer, K. Steiglitz, and P. Prucnal, "Observation of temporal vector soliton propagation and collision in birefringent fiber," Phys. Rev. Lett. **98**, 053902 (2007).
7. B. Frisquet, B. Kibler, and G. Millot, "Collision of Akhmediev breathers in nonlinear fiber optics," Phys. Rev. X **3**, 041032 (2013).
8. R. Radhakrishnan, M. Lakshmanan, and J. Hietarinta, "Inelastic collision and switching of coupled bright solitons in optical fibers," Phys. Rev. E **56**, 2213–2216 (1997).
9. T. Kanna, M. Lakshmanan, P. Dinda, and N. Akhmediev, "Soliton collisions with shape change by intensity redistribution in mixed coupled nonlinear Schrödinger equations," Phys. Rev. E **73**, 026604 (2006).
10. J. Yang and Y. Tan, "Fractal structure in the collision of vector solitons," Phys. Rev. Lett. **85**, 3624–3627 (2000).
11. M. Jakubowski, K. Steiglitz, and R. Squier, "State transformations of colliding optical solitons and possible application to computation in bulk media," Phys. Rev. E **58**, 6752–6758 (1998).
12. K. Steiglitz, "Time-gated Manakov spatial solitons are computationally universal," Phys. Rev. E **63**, 016608 (2000).
13. R. Goodman and R. Haberman, "Vector-soliton collision dynamics in nonlinear optical fibers," Phys. Rev. E **71**, 056605 (2005).
14. C. Liu, Z. Yang, L. Zhao, and W. Yang, "Vector breathers and the inelastic interaction in a three-mode nonlinear optical fiber," Phys. Rev. A **89**, 055803 (2014).
15. X. Zhao, T. Li, Y. Liu, Q. Li, and Z. Zheng, "Polarization-multiplexed, dual-comb all-fiber mode-locked laser," Photon. Res. **6**, 853–857 (2018).
16. G. Herink, F. Kurtz, B. Jalali, D. Solli, and C. Roppers, "Real-time spectral interferometry probes the internal dynamics of femtosecond soliton molecules," Science **356**, 50–54 (2017).
17. K. Krupa, K. Nithyanandan, U. Andral, P. Dinda, and P. Grelu, "Real-time observation of internal motion within ultrafast dissipative optical soliton molecules," Phys. Rev. Lett. **118**, 243901 (2017).
18. X. Liu, X. Yao, and Y. Cui, "Real-time observation of the buildup of soliton molecules," Phys. Rev. Lett. **121**, 023905 (2018).
19. J. Peng and H. Zeng, "Build-up of dissipative optical soliton molecules via diverse soliton interactions," Laser Photon. Rev. **12**, 1800009 (2018).
20. G. Herink, B. Jalali, C. Ropers, and D. Solli, "Resolving the build-up of femtosecond mode-locking with single-shot spectroscopy at 90 MHz frame rate," Nat. Photonics **10**, 321–326 (2016).
21. X. Liu and Y. Cui, "Revealing the behavior of soliton buildup in a mode-locked laser," Adv. Photon. **1**, 016003 (2019).
22. X. Liu and M. Pang, "Revealing the buildup dynamics of harmonic mode-locking states in ultrafast lasers," Laser Photon. Rev. **13**, 1800333 (2019).
23. A. Runge, N. Broderick, and M. Erkintalo, "Observation of soliton explosions in a passively mode-locked fiber laser," Optica **2**, 36–39 (2015).
24. J. Peng and H. Zeng, "Soliton collision induced explosions in a mode-locked fiber laser," Commun. Phys. **2**, 34 (2019).
25. M. Liu, A. Luo, Y. Yan, S. Hu, Y. Liu, H. Cui, Z. Luo, and W. Xu, "Successive soliton explosions in an ultrafast fiber laser," Opt. Lett. **41**, 1181–1184 (2016).
26. P. Wang, X. Xiao, H. Zhao, and C. Yang, "Observation of duration-tunable soliton explosion in passively mode-locked fiber laser," IEEE Photon. J. **9**, 1507008 (2017).
27. Y. Wei, B. Li, X. Wei, Y. Yu, and K. K. Y. Wong, "Ultrafast spectral dynamics of dual-color-soliton intracavity collision in a mode-locked fiber laser," Appl. Phys. Lett. **112**, 081104 (2018).
28. M. Liu, T. Li, A. Luo, W. Xu, and Z. Luo, ""Periodic" soliton explosions in a dual-wavelength mode-locked Yb-doped fiber laser," Photon. Res. **8**, 246–251 (2020).
29. K. Zhao, C. Gao, X. Xiao, and C. Yang, "Buildup dynamics of asynchronous vector solitons in a polarization-multiplexed dual-comb fiber laser," Opt. Lett. **45**, 4040–4043 (2020).
30. J. Guo, K. Zhao, B. Zhou, W. Ning, K. Jiang, C. Yang, L. Kong, and Q. Dai, "Wearable and skin-mountable fiber-optic strain sensors interrogated by a free-running, dual-comb fiber laser," Adv. Opt. Mater. **7**, 1900086 (2019).
31. K. Zhao, H. Jia, P. Wang, J. Guo, X. Xiao, and C. Yang, "Free-running dual-comb fiber laser mode-locked by nonlinear multimode interference," Opt. Lett. **44**, 4323–4326 (2019).
32. L. A. Sterczewski, A. Przewloka, W. Kaszub, and J. Sotor, "Computational Doppler-limited dual-comb spectroscopy with a free-running all-fiber laser," APL Photon. **4**, 116102 (2019).
33. G. Wang, G. Chen, W. Li, and C. Zeng, "Real-time evolution dynamics of double-pulse mode-locking," IEEE J. Sel. Top. Quantum Electron. **25**, 1100504 (2019).
34. M. Liu, H. Chen, A. Luo, G. Zhou, Z. Luo, and W. Xu, "Identification of coherent and incoherent spectral sidebands in an ultrafast fiber laser," IEEE J. Sel. Top. Quantum Electron. **24**, 1100606 (2017).
35. D. Tang, H. Zhang, H. Zhao, L. Zhao, and X. Wu, "Observation of high-order polarization-locked vector solitons in a fiber laser," Phys. Rev. Lett. **101**, 153904 (2008).
36. H. Zhang, D. Tang, L. Zhao, and H. Tam, "Induced solitons formed by cross-polarization coupling in a birefringent cavity fiber laser," Opt. Lett. **33**, 2317–2319 (2008).
37. M. Dennis and I. Duling, "Experimental study of sideband generation in femtosecond fiber lasers," IEEE J. Quantum Electron. **30**, 1469–1477 (1994).
38. H. Zhang, D. Tang, L. Zhao, and N. Xiang, "Coherent energy exchange between components of a vector soliton in fiber lasers," Opt. Express **16**, 12618–12623 (2008).
39. L. Zhao, D. Tang, X. Wu, H. Zhang, C. Lu, and H. Tam, "Observation of dip-type sidebands in a soliton fiber laser," Opt. Commun. **283**, 340–343 (2010).
40. Y. Du, Z. Xu, and X. Shu, "Spatio-spectral dynamics of the pulsating dissipative solitons in a normal-dispersion fiber laser," Opt. Lett. **43**, 3602–3605 (2018).
41. Z. Wei, M. Liu, S. Ming, A. Luo, W. Xu, and Z. Luo, "Pulsating soliton with chaotic behavior in a fiber laser," Opt. Lett. **43**, 5965–5968 (2018).
42. J. Peng, S. Boscolo, Z. Zhao, and H. Zeng, "Breathing dissipative solitons in mode-locked fiber lasers," Sci. Adv. **5**, eaax1110 (2019).
43. G. Ycas, F. R. Giorgetta, E. Baumann, I. Coddington, D. Herman, S. A. Diddams, and N. R. Newbury, "High-coherence mid-infrared dual-comb spectroscopy spanning 2.6 to 5.2 μm," Nat. Photonics **12**, 202–208 (2018).